Printable all-dielectric water-based absorber

Patrick J. Bradley[1,2*], **Max O. Munoz Torrico**[1], **Conor Brennan**[2], **and Yang Hao**[1]

[1]School of Electronic Engineering and Computer Science, Queen Mary University of London, London, E1 4NS, UK
[2]School of Electronic Engineering, Dublin City University, Dublin, D09 W6Y4, Ireland
[*]p.bradley@qmul.ac.uk; y.hao@qmul.ac.uk

Supplementary Information

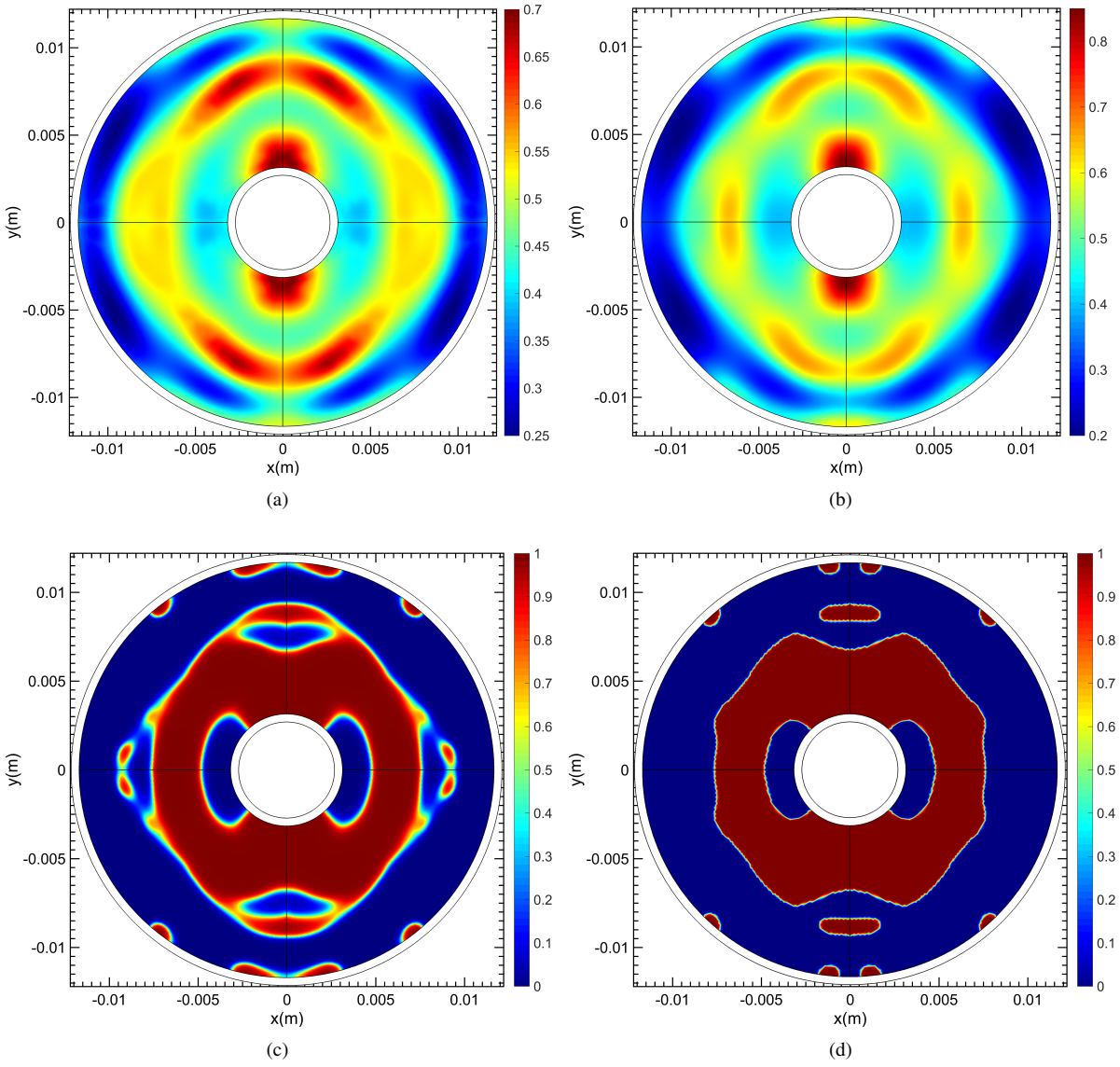


Figure 1. Projected filtered density value $\overline{\rho}(\rho)$ at 4 discrete iteration cycles, where unity indicate a seed permittivity (water) and zero, the parent (VeroClear). a, Iteration 100 **b**, 200 **c**, 400 **d**, final iteration 600 with a final seed volume fraction of 38%.

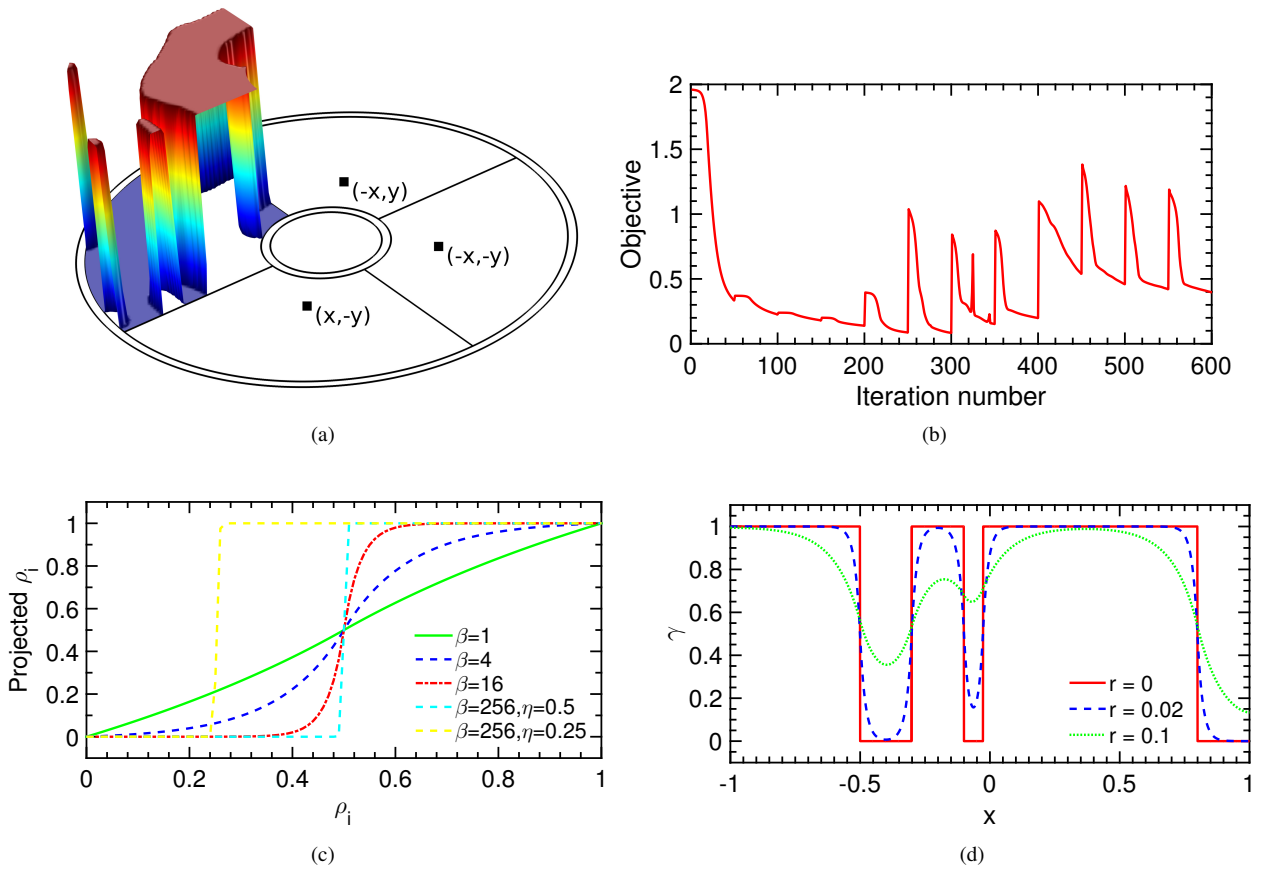


Figure 2. Topology optimisation convergence and control parameters plots. a, projected filtered density value $\tilde{\rho}$ at final iteration for a single quadrant, which undergo a 90, 180 and 270 degree clockwise rotation transformation ensuring symmetric and angular independent absorption. **b**, convergence plot of optimisation objective function, manifestation of doubling the projection parameter β every 50^{th} iteration is evident **c** the projected physical density function controlled by β to ensure smooth convergence by a controlled projection of the filtered density value $\widetilde{\rho}$ to a binary solution **d**, and Helmholtz PDE density filter example for 1D input comparing effect of different length parameters r.

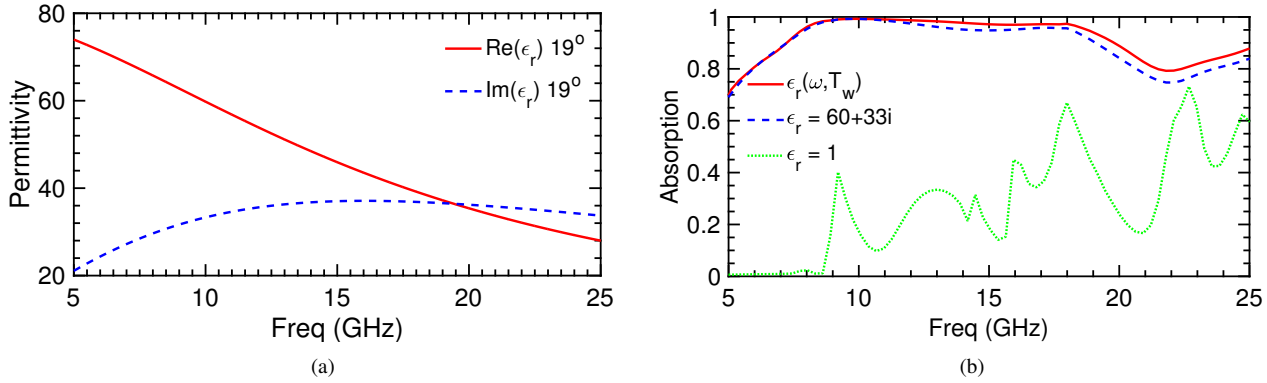


Figure 3. Dielectric profile water and absorption as a function of permittivity. a, thermal and frequency dependent profile of water permittivity for 19^o as used in the optimisation sequence and as defined in the Method section. **b**, absorption as a function of seed permittivity comparing water (**red**) as defined above vs an averaged uniform permittivity of $\varepsilon_r = 60 + 33\imath$ (**blue**) with that of replacing water with air (**green**), indicating switchability of our device from absorption to transmission.

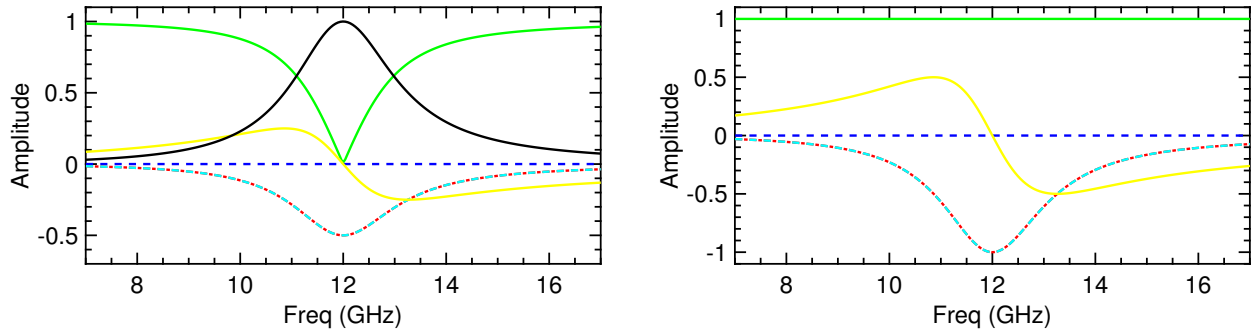


Figure 4. Analytical results for spectral overlapping electric and magnetic resonance of equal strength and width for an ideal loss-less metamaterial, demonstrating the effect of changing the magnitude of these resonances in tandem and extracted theoretical electric and magnetic dipole responses. a, consequence of real part of the electric (**red**) and magnetic (**cyan**) resonances being equal to negative half of the incident field amplitude, therein, we observe a flat line reflection (**blue**) with zero transmission (**green**) and perfect absorption (**black**) of unity. **b**, correspondingly, if we double the electric (**red**) and magnetic (**cyan**) resonances we move from perfect absorption at a single frequency to perfect unity transmission (**green**).

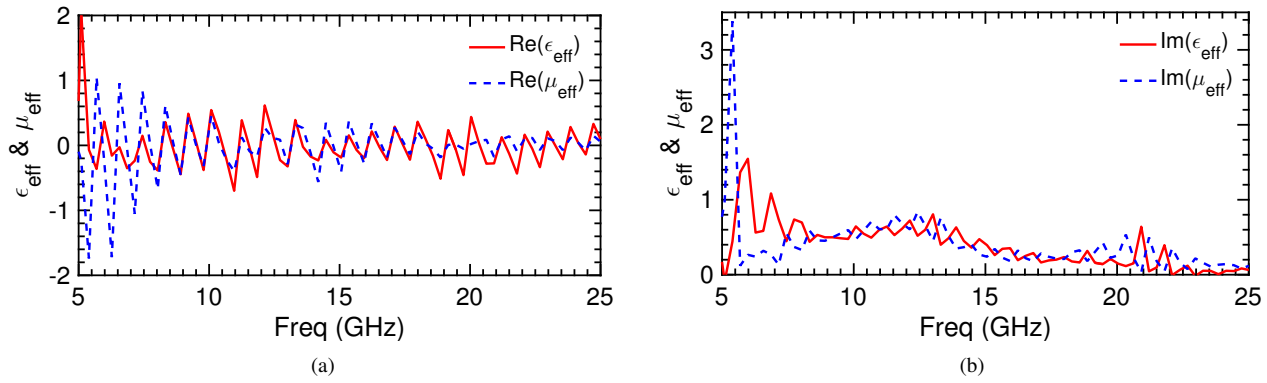
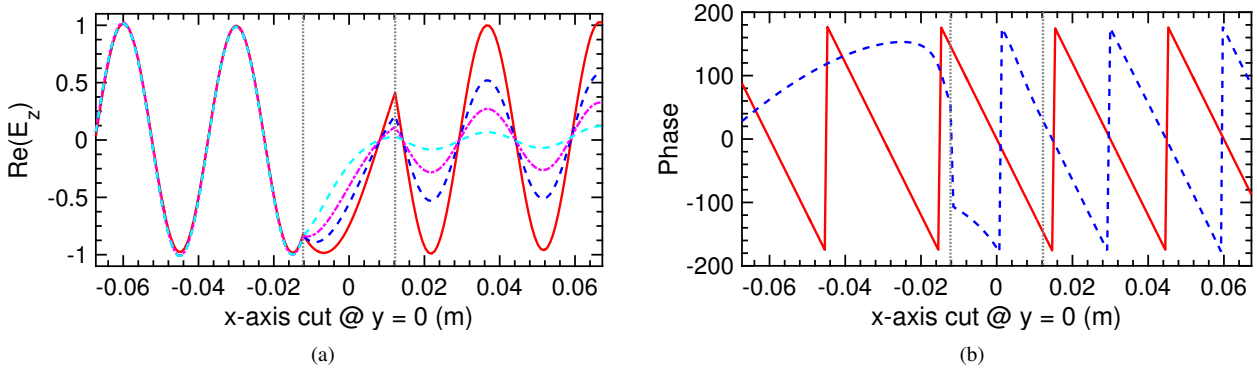
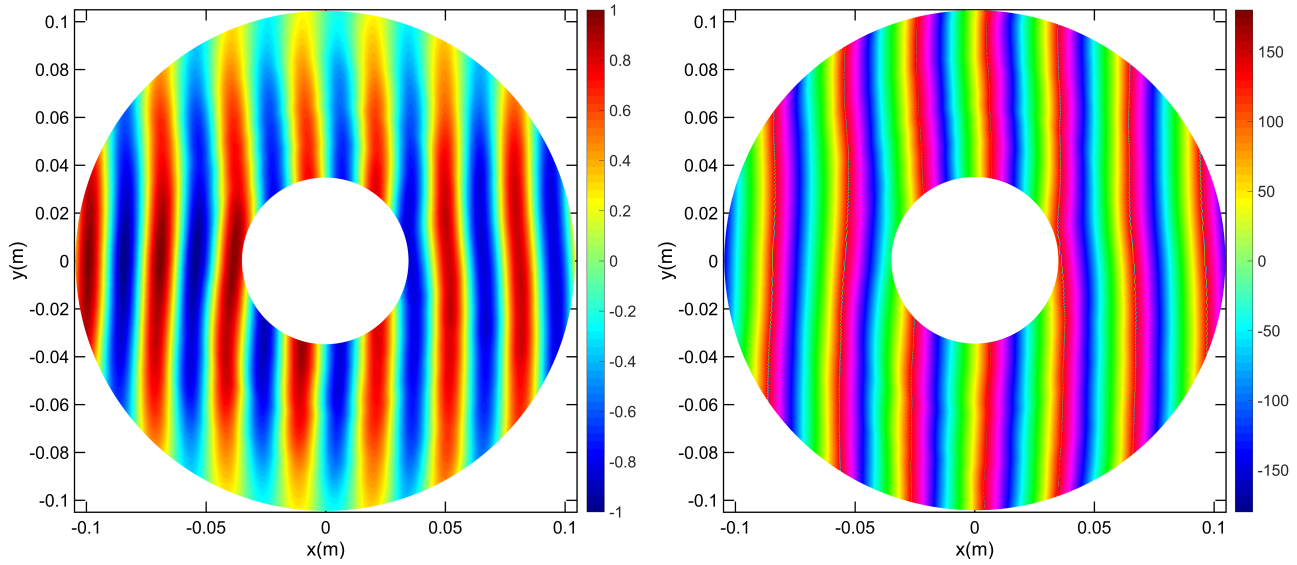


Figure 5. Extracted effective material coefficients from simulated S-parameters for normally incident plane wave. a, real part of the inverted effective permittivity (**red**) and permeability (**blue**) **b**, related imaginary components.



(a) (b)

Figure 6. Line cut of electric field along the x-axis @ y=0 where the cylindrical array has been replaced with the equivalent constant medium. a normalized electric field values for 4 difference vales of loss for an equivalent homogeneous medium with thickness 24.45 mm, where grey lines indicate boundary of the medium at 10 GHz, $n = -0.5 + 0.5\imath$ (**cyan** - averaged extracted refractive index), $n = -0.5 + 0\imath$ (**red**), $-0.5 + 0.125\imath$ (**blue**) and $-0.5 + 2\imath$ (**magenta**). This plot illustrates the conditions required to observe a near-unity incident and near-zero transmission along the x-axis @ y=0. **b**, associated phase of incident (**red**) and scattered electric field (**blue**) for same equivalent media with $n = -0.5 + 0.5\imath$ at 10 GHz. In this arrangement, destructive interference between the two waves of equal amplitude but π-path delay take place in the forward direction, resulting in cancellation of the total electric field ensuring zero transmission as predicted by theory



(a) (b)

Figure 7. Normalised free space measurements probed within a parallel plate waveguide chamber at 10GHz which facilitate the normalisation of all subsequent measured electric fields to the free space. a, measured real component **b**, and corresponding phase of the total electric field. Measurements were probed within a 5mm radial, 0.25^o angular resolution and interpolated using a linear function. The chamber was excited by a rectangular x-band waveguide and converted to a normally incident plane wave by a cylindrical-to-plane wave transformer lens as described in Method section.

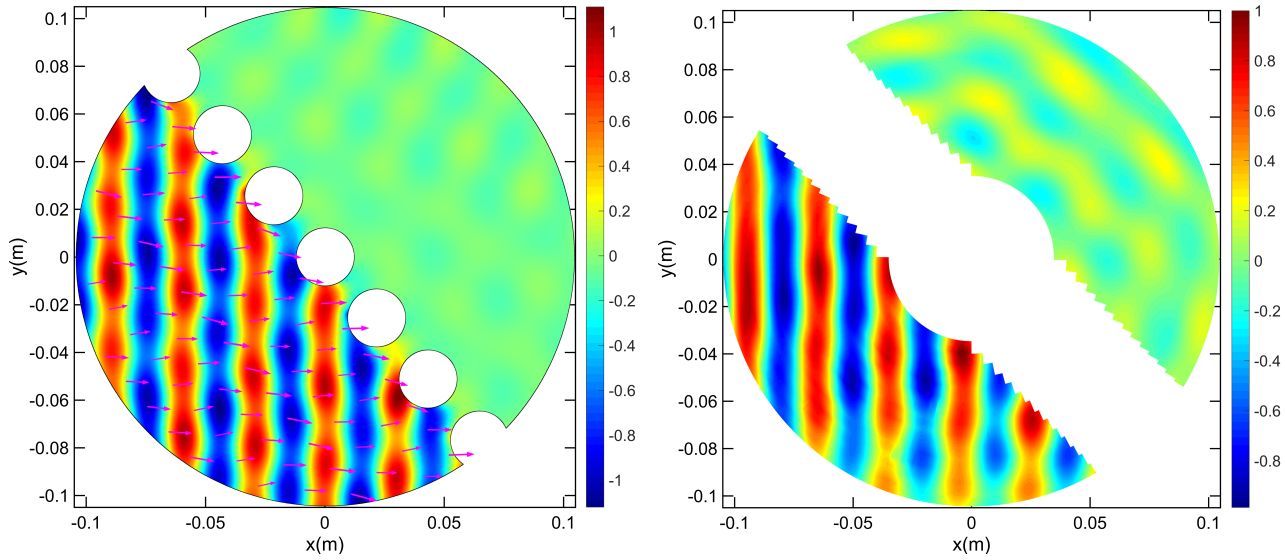


Figure 8. Simulated and measured real component of total electric field, z component (V/m), normalised to free space and power flow time average arrow plot at varying frequencies for a 45^o incident plane wave excitation at 10 GHz with 7 cylindrical absorbers periodical arranged along the y-axis @ x = 0. a, simulated electric field and power flow time average arrow plot **b**, associated measured results for same set-up.

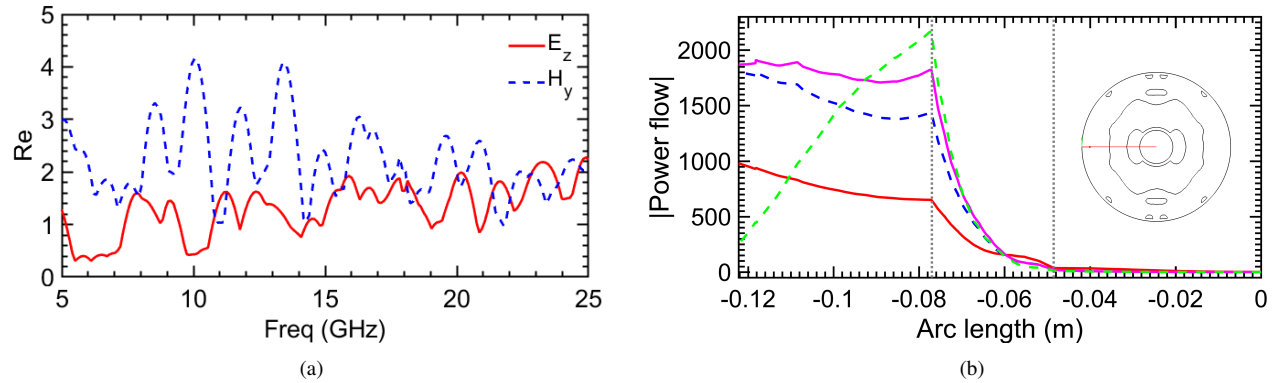


Figure 9. Simulated results for the surface electric field, magnetic field and power flow time average within the cylinder design boundary. a, real component of the electric in z (**red**) and magnetic in y (**blue**) surface maximum values normalised to free space, which illustrate the complexity of the electric and magnetic enhancements across the frequency spectrum of interest. **b**, simulated power flow time average x component extracted from along the x-axis @ y=0 as per insert, where grey lines indicate boundary of the water medium recorded at key electric and magnetic surface maxima's, 7.82 (**red** 1), 12.37 (**magenta** 2), 13.48 (**blue** 3) and 16.31 (**green** 4) GHz.

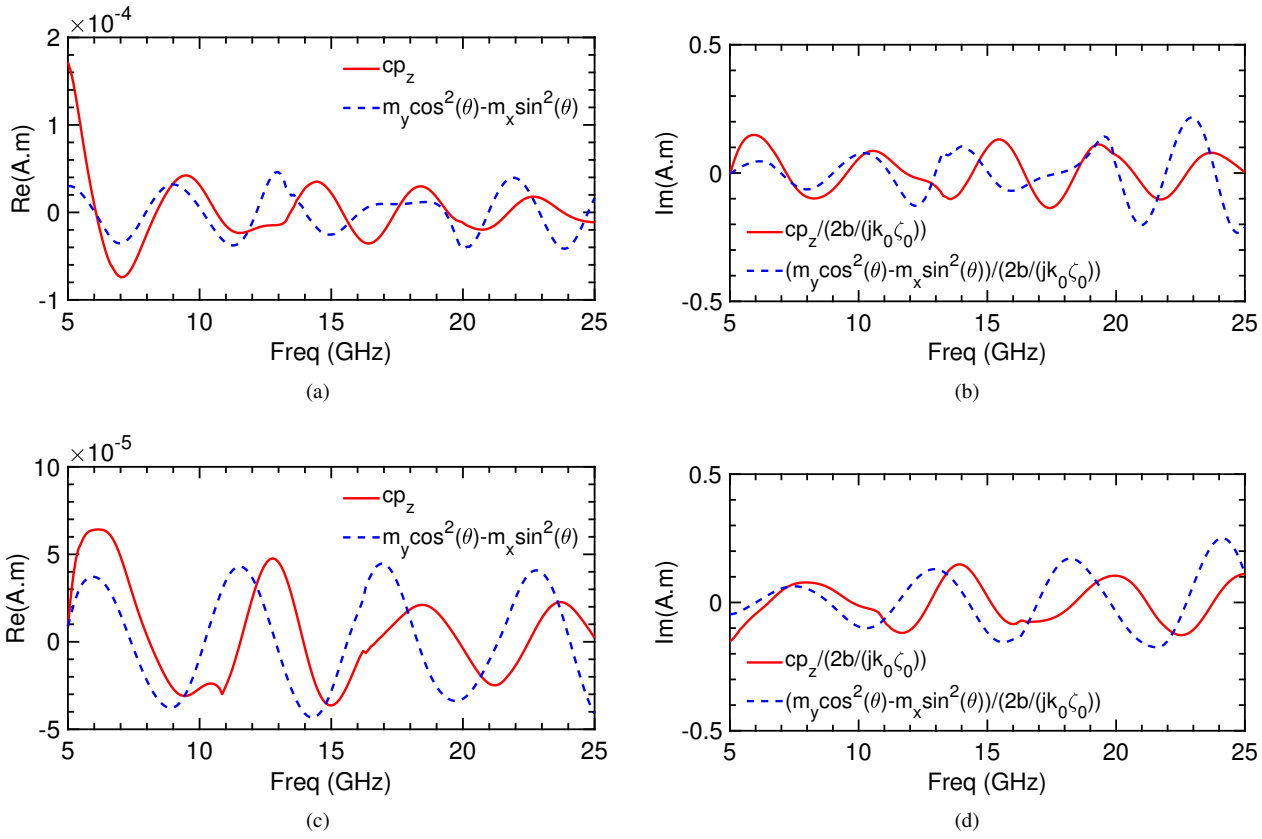


Figure 10. Simulated extracted equivalent moment for absorber design subject to a 20 and 40 degree plane wave incidence. a,c, Real and **b,d**, scaled imaginary component of the electric (**red**) and magnetic (**blue**) dipole moment resonances for 20 and 40 degree incidence respectively, where a zero response fulfils the theoretical case for perfect absorption.

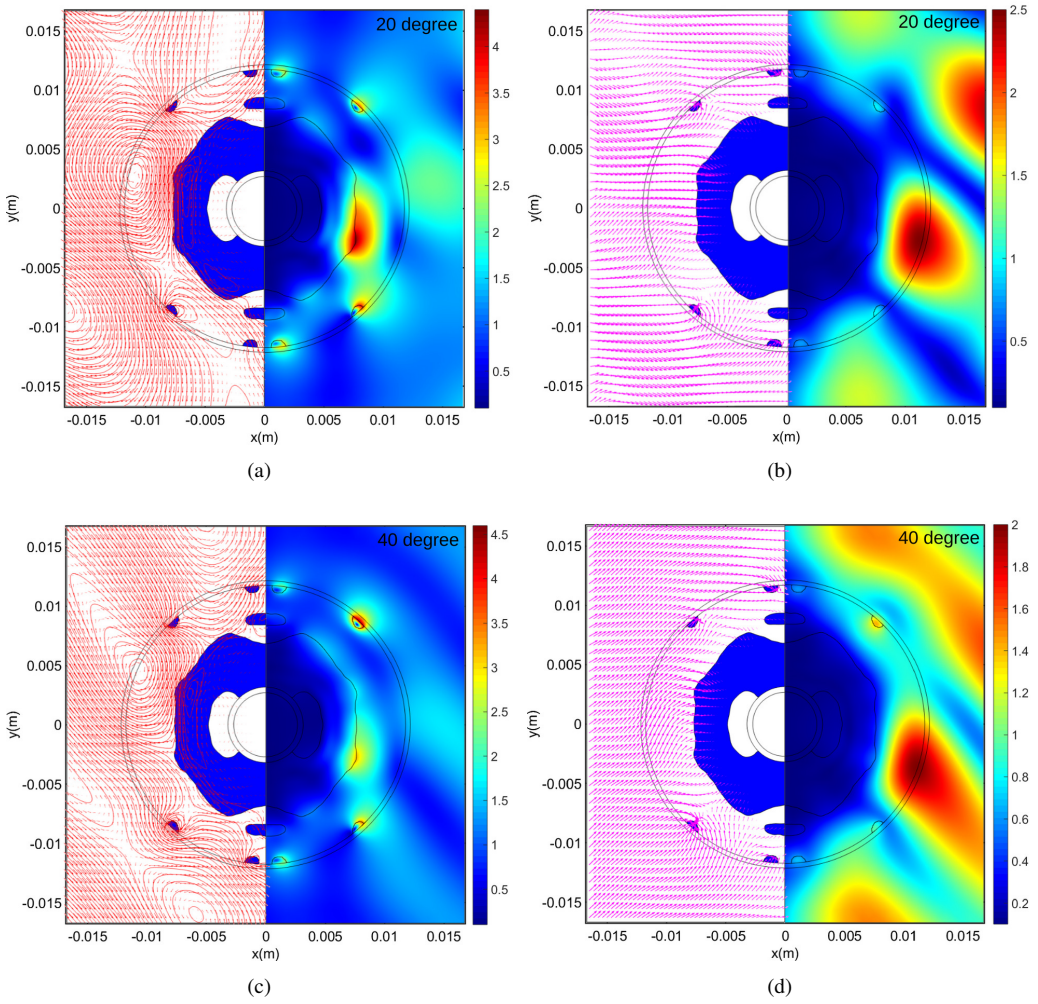


Figure 11. Simulated surface magnetic, power flow time average and electric field amplitude plots normalised to free space at 13.48 GHz for two discrete incident angles. a,c -x illustrates logarithmic scaled surface arrow & streamlines for the *x* and *y* magnetic field components at 20 and 40-degree illumination indent from LH boundary, +x 180^o rotated image of the corresponding magnetic field magnitude. **b,d** -x illustrates related logarithmic scaled power flow time average arrow and +x the 180^o rotated electric field magnitudes. As the incident field rotates there is a corresponding shift in the magnetic modes orientation. However, as expected, the magnetic field magnitude remains nearly unchanged from normal incidence due to the balancing of *y* magnetic components with its *x* contribution. Together with Figs. 10(a)-10(d) these plots provide valuable insight into the nature of the angular stability.